

Chapter 5

Study of timing and spectral properties of Be/X-ray pulsar 4U 1901+03

5.1 Introduction

The Be X-ray pulsar 4U 1901+03 was discovered by Uhuru in 1970-1971. The pulse period of the pulsar was about ~ 2.76 s. The pulsating nature of the source was discovered in 2003 (Galloway *et al.*, 2005). The orbital period of the pulsar is 22.58 days. Large negative residuals near 10 keV (10 keV feature) have been observed in the spectrum of the source

The objective of the investigation here is to investigate the 10 keV feature present in the spectrum in detail. The variation of 10 keV feature with pulse phase and luminosity are also studied. In addition to that we have also studied the 30 keV feature and its variation with pulse phase. We have discussed in detail the possible reason behind the origin of these features. The detail discussion on the variation of the pulse profiles of 4U 1901+03 with time and energy are also presented.

A part of this chapter is accepted for publication in *Astrophys. Space Sci* ASTR-D-20-00586R2.

5.2 Observation and Data reduction

NuSTAR

The *Nuclear Spectroscopic Telescope Array (NuSTAR)* observed the Be/X-ray pulsar 4U 1901+03 four times during the 2019 outbursts. As discussed earlier *NuSTAR* consists of two focusing telescopes which operates in 3-79 keV energy range, each of them have their own focal plane module consisting of CdZnTe detector. The data reduction were done using HEASOFT v6.26.1. The mission specific FTOOL nupipeline was used to obtain clean event file from the unfiltered event file. From this cleaned event file we have extracted the source and background regions. With the help of xselect, the image obtained from the cleaned event file is plotted in DS9. A circular region of radius 90'' along the direction of the source was considered as a source region and another circular region of same radius but in the direction away from the source was taken as the background region. For both the focal plane modules FPMA & B, the region files were extracted. Using this region files the final product *i.e.* spectra and light curves, were then obtained with the help of *nuproducts*. The background correction of the light curves are done using lcmath. The background corrected light curves from the two focal plane modules were combined using the same tool. After that the barycentric correction were made with the help of barycorr using the telescope orbit file. From hereafter we are going to refer the four *NuSTAR* observations by Obs1, Obs2, Obs3 and Obs4 respectively.

Swift

Swift observed the source multiple times during the outburst. We have used *Swift*-XRT data for our analysis. The standard data processing and screening were done using xrtpipeline. We have only considered the *Swift*-XRT observations done in Window Timing (WT) mode having good timing resolution for the timing analysis. The cleaned event file was extract in

xselect and the image was plotted in DS9. From the plotted clean image a circular region of radius 20 pixel around the optical position of the source is considered as the source region. An another circular region of same radius but far away from the optical center was taken as the background region. Using these region files in xselect we extracted source and background light curves and spectra. The ancillary response file (ARF) required for the spectral analysis of the spectrum was created using the *Swift* mission specific tool `xrtmkarf`. The response matrices file (RMF) was obtained from the latest calibration database files. The background correction was done using `lcmath`. The background corrected light curves have been further corrected from the telescope vignetting and point spread function using the `xrtlccorr`. After 58637.08 MJD *Swift* observations were made in photon counting (PC) mode and the source was visible only in one observation. Finally the barycentric correction was made using `barycorr`.

NICER

To study the variation in the shape of the pulse profiles after 58637.08 MJD we have used data from NICER observations of the pulsar. The standard data screening and filtering in this case was done using the standard NICER pipeline processing tool `nicerl2`. From the clean event file light curves in 0.2-12 keV energy range having a binning of 1 ms are extracted. As NICER is a non-imaging detector so the background light curves cannot be known here consequently the light curves obtained here is not background corrected. However barycentric correction of the light curves can be made here using the tool `barycorr`.

Table 5.1 Table showing four *NuSTAR* observations indicated by their observation IDs along with the date of observation, exposure and the pulse period of pulsar.

obsId	Date of Obs (MJD)	Exposure (ks)	P_s
90501305001	58531.121	17.85	2.764 ± 0.003
90502307002	58549.308	12.25	2.762 ± 0.003
90502307004	58584.946	21.45	2.762 ± 0.001
90501324002	58615.752	45.12	2.760 ± 0.001

5.3 Analysis and Results

5.3.1 Light curves

The four horizontal lines along with the down arrow in Fig. 5.1 represents the four *NuSTAR* observations taken during different stages of the outburst. Flares are seen in the light curves of all the four *NuSTAR* observations. Flare is considered to be a part of the light curve having count rate 3σ level above the mean value. We have found that for the first two observations the mean number of flares per hour was 5-6 and for the last two observations it was 3-4 flares per hour. The duration of the flares were from few tens to hundreds of seconds. To estimate the duration of the flares we have taken the beginning and the end of the flares described by the lowest point of the flares below that of the mean value. For the first observation the mean duration of the burst was ~ 135 s, whereas for the second observation it was ~ 62.18 s. For the last two observations, the mean duration were ~ 98.13 s and 95.35 s (Fig. 5.2).

5.3.2 Pulse Profiles and Pulse Fraction

The pulse periods of the pulsar were estimated crudely making use of the `ftool powspec`, which transforms the light curves into the Fourier components. For the *NuSTAR* observation, we have taken the light curves having binning of 1 ms to estimate the pulse periods and hence obtained the pulse profiles. Using `efsearch` the final estimation of the pulse period was done. The pulse periods of the four *NuSTAR* observations is shown in Table 5.1.

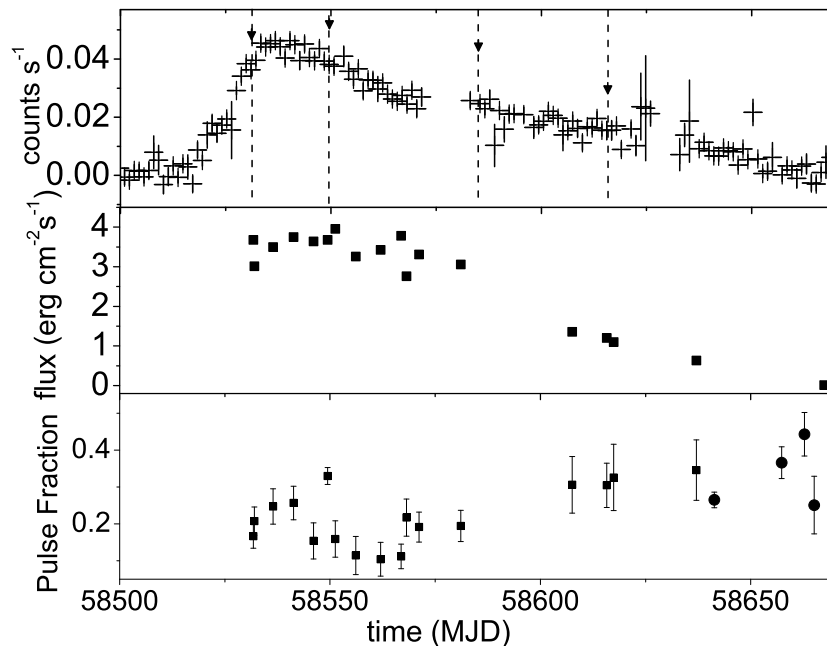


Fig. 5.1 Upper panel shows *Swift*-BAT light curves of 4U 1901+03 during 2019 outburst in 15-50 keV energy range. The down arrows and vertical lines indicates four *NuSTAR* observations. The middle panel shows variation of *Swift*-XRT flux in 0.5-10 keV energy range. Fluxes are in the order of 10^{-9} and obtained by using the command flux in XSPEC for *Swift*-XRT spectra fitted by POWERLAW model. Bottom panel represents change in Pulse fraction with time, the square and circle symbols are for *Swift*-XRT (0.5-10.0 keV) and NICER (0.2-12 keV) respectively.

The uncertainty in the pulse period was determined by the method used in Boldin *et al.* (2013). In this method the errors is determined by the so-called bootstrap method, where we have generated the light curves starting from the initial light curve using the formula $r'_i = r_i + \gamma\sigma_{r_i}$, where r'_i and r_i are the i^{th} count rates of the new and the original light curves respectively, where γ represents a quantity distributed between -1 and +1 and σ_{r_i} represents the error associated with the i^{th} flux measurement. The pulse period from the new light curve is also determined using *efsearch*. The process is repeated for $N = 1000$ times and determined the pulse period (P_i) in each case. The mean pulse period $\langle P \rangle$ corresponds to most probable period and the standard deviation (σ_P) is the associated error of the pulse period. The pulse period of the 4U 1901+03 is found to vary throughout the outburst. The variation of pulse period during the outburst can be due to the transfer of the angular

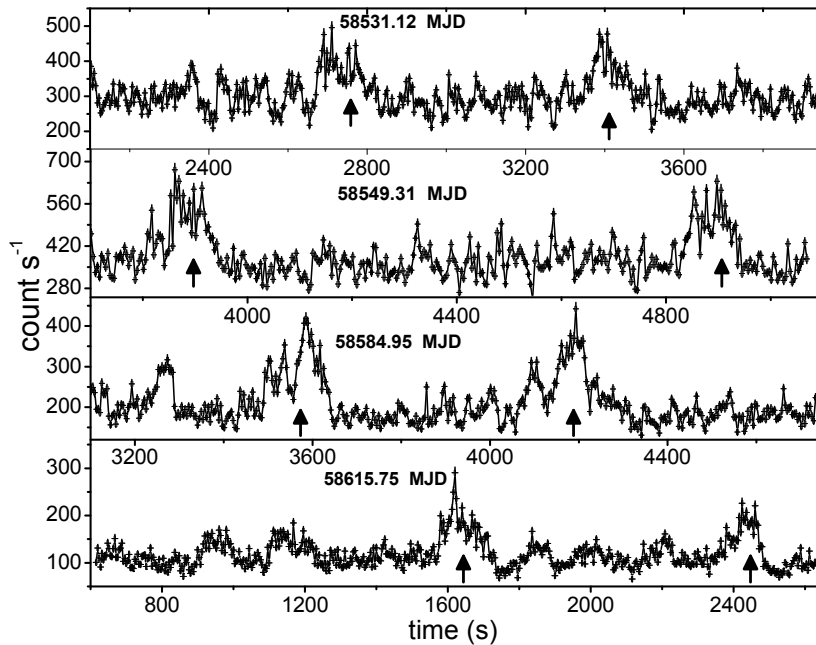


Fig. 5.2 Light curves showing some of the bursts observed in four *NuSTAR* observations. The burst present in the light curves is indicated by up arrow.

momentum onto the neutron star from the accretion disk (Ghosh and Lamb, 1979; Wang, 1987). As a result of transfer of angular momentum there will be an accelerating torque acting on to the neutron star. It is this accelerating torque which causes the intrinsic spin or the pulse period of a X-ray pulsar to vary. Pulse profiles are then obtained by folding the light curve about the given pulse period. For *Swift*-XRT the light curves of binning 1.8 ms are used to extract both the pulse periods and the pulse profiles.

It is evident from the analysis that the pulse profile of the pulsar varies throughout the outburst. The pulse profile during the first *NuSTAR* observation at 58531.121 MJD in the energy range 3-79 keV follow a sinusoidal shape (Fig. 5.3) which later evolved into double peaked at 58549.308 MJD having a main peak. After that it again changed to a single peak with a notch at a phase 0.5 at 58584.946 MJD. During the last *NuSTAR* observation at 58615.752 MJD the pulse profile in 3-79 keV energy range was found to have a single peak similar to that of the first observation but it is little sharper than from that of the first observation. We also studied the temporal variation of the pulse profile using *Swift*-XRT

observations. The variation of the pulse profile is plotted in Fig. 5.4. It is evident that the pulse profile at 58532.03 MJD is double peaked with one major primary peak. The second peak is found to merge with the primary at 58541.33 MJD, which subsequently evolved into single peaked with a notch at 58568.16 MJD later. The pulse profile became broad single peaked at 58581.05 MJD. In between 58607.54-58637.08 MJD the pulse profiles are found having broad single peak. However the pulse profile observed at 58665.09 MJD using NICER observation is found to have single peak which is very sharp compared to that of the *Swift*-XRT. However, no further pulsation observed after 58665.09 MJD.

To study the dependence of the pulse profiles on energy, we have extracted the light curves in different energy bands for the *NuSTAR* observations. The following energy ranges 3-7 keV, 7-12 keV, 12-18 keV, 18-24 keV and 24-32 keV have been chosen for this purpose. For Obs1, the pulse profiles at different energy bands are almost sinusoidal in shape (Fig. 5.3). For this observation the pulse profiles in the energy bands 7-12 keV and 3-79 keV are found almost similar. In the hard X-ray region above 12 keV an increase in the height of the pulse profiles has been observed. For Obs2, pulse profiles in 3-7 keV, 7-12 keV, 12-18 keV and 3-79 keV, we observed existence of double peaks which however differs in shape. It is observed that the second peak was absent in the pulse profiles for the energy ranges 18-24 keV and 24-32 keV. It is observed here that the height of the primary peak has increased in these energy bands. In the energy bands 3-7 keV and 3-79 keV, the pulse profiles for Obs3 are found to have nearly single peak with a notch near ~ 0.5 , however, above 7 keV the pulse profiles are not so smooth, which are associated with large errors. Above 24 keV energy no clear peak was visible. In the case of Obs4, the pulse profiles at different energy bands are found to have almost sinusoidal shape, pulse profiles in the energy bands 7-12 keV and 3-79 keV are almost similar, however, above 18 keV we note large errors associated with each of the normalized count rates.

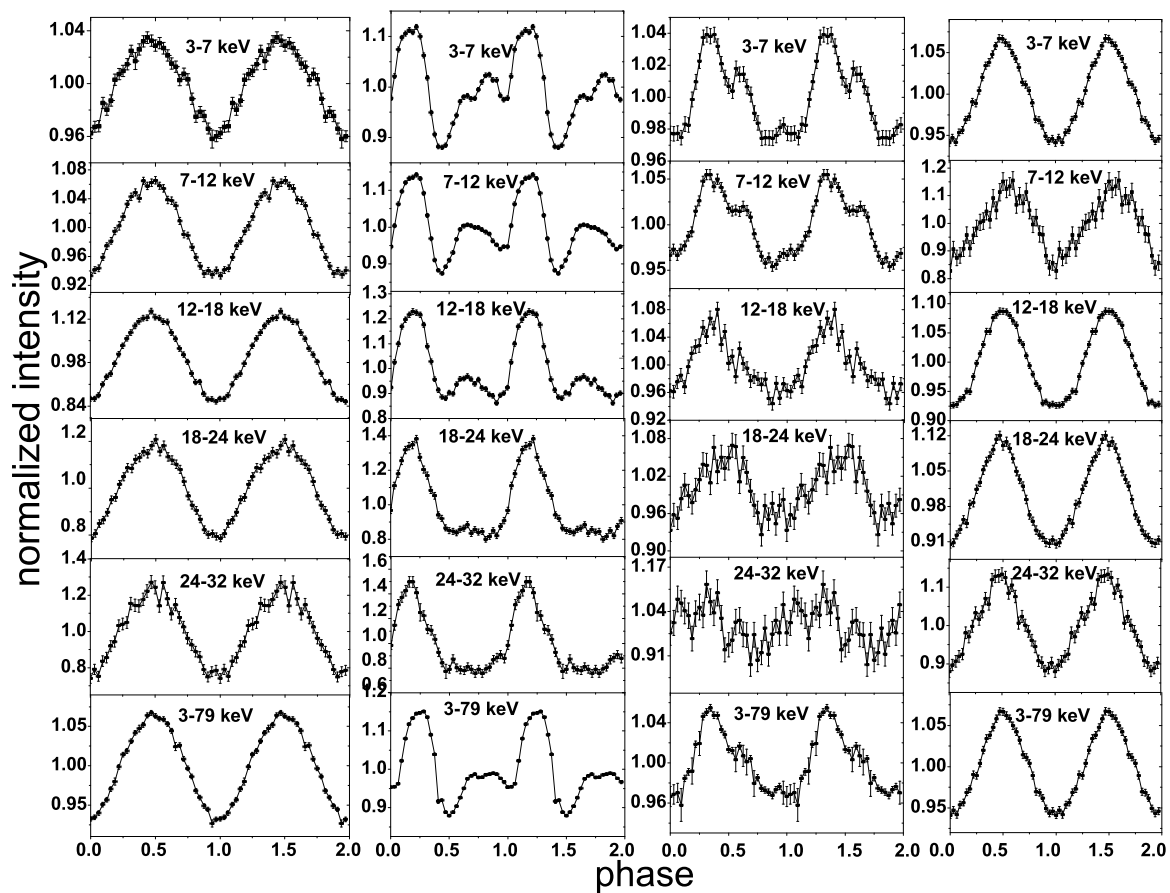


Fig. 5.3 Pulse profiles for different *NuSTAR* observations and variation of pulse profile with energies. Figures (a), (b), (c) and (d) are for the 58531.12, 58549.31, 58584.95 and 58615.75 MJD respectively.

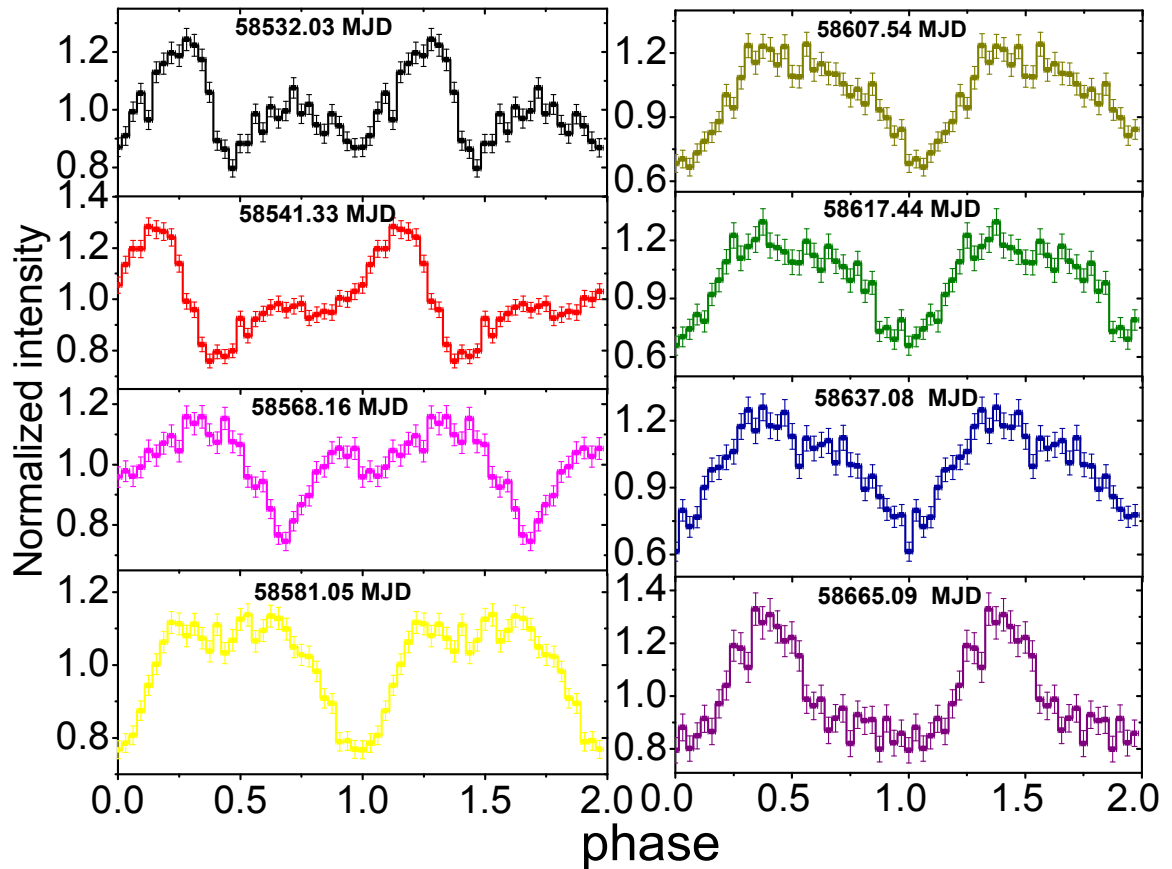


Fig. 5.4 Variation of Pulse profile with time. Pulse profiles from 58532.03 to 58637.08 MJD are obtained by folding *Swift*-XRT lightcurve. For *Swift*-XRT the significant level of pulse periods were greater than 3σ . The broadening of the *Swift*-XRT pulse profiles can be due to the short exposure time of the instrument so that there is not enough photons count rate to fold about the pulse period. The last pulse profile at 58665.09 MJD is obtained by folding NICER lightcurve in 0.2-12 keV energy range (Obs Id - 2200570141).

The pulse fraction (PF) of a pulsar is defined as $PF = \frac{p_{max} - p_{min}}{p_{max} + p_{min}}$, where p_{max} and p_{min} are the maximum and minimum intensities associated with that of the pulse profile respectively. In Fig. 5.5, PF is plotted with respect to energy for the four *NuSTAR* observations. The pulse fraction of the pulsar is found to increase with the energy in all the four *NuSTAR* observations. For Obs1 pulse fraction shows almost a monotonic increase with the increase in energy (black). Pulse fractions increases slowly between 5-15 keV but above 15 keV pulse fraction increases rapidly (red) in the case of Obs2. In the third observation (blue) pulse fractions increases slowly between 5-12 keV and found to have almost constant value between 12-21 keV, above 21 keV pulse fraction is observed to increase once again. In Obs4 pulse fractions increases between 5-25 keV which remains almost constant above 25 keV. From the Fig. 5.5, it is clear that the variation of the pulse fraction with the energy is steep for the first two observations. The luminosity in the case of the first two observations were higher than the last two observations. Thus the pulse fraction in different energy ranges is high if the luminosity is high. The variation of the pulse fraction with energy for different *NuSTAR* observations displayed in Table 5.2.

The variation of the pulse fraction with time and flux are studied using *Swift*-XRT observations. The pulse fraction was found to increase initially between 58531.77-58549.43 MJD from 0.17-0.33 and thereafter decreases to 0.16 at 58551.23 MJD which remains almost constant between 58556.14-58566.91 MJD. However in between 58568.16-58637.08 MJD, the pulse fraction increases from 0.22 to 0.34 (bottom panel of Fig. 5.1). The variation of the pulse fraction with the flux in 0.5-10 keV energy range is shown in the bottom panel of Fig. 5.9. The pulse fraction decreases from 0.34-0.10 as flux increases from $0.64-3.43 \times 10^{-9}$ erg cm⁻² s⁻¹, which is found to increase from 0.11 to 0.33 between $3.43-3.68 \times 10^{-9}$ erg cm⁻² s⁻¹ and then abruptly decreases one again to 0.15 at 3.96×10^{-9} erg cm⁻² s⁻¹. Thus as we study for flux below 3.43×10^{-9} erg cm⁻² s⁻¹, it is found that

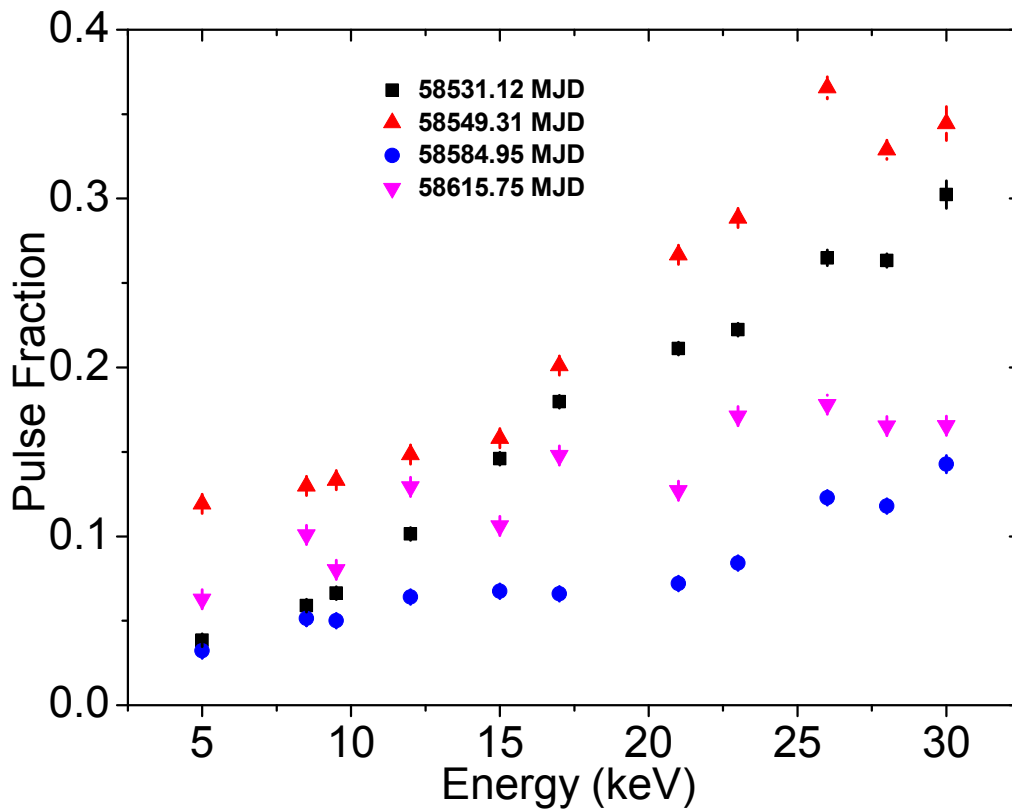


Fig. 5.5 Variation of the pulse fraction of the pulse profile with energy obtained using *NuSTAR* observations. The first, second, third and fourth columns are for Obs1, Obs2, Obs3 and Obs4 respectively.

there is an increase in the pulse fraction. Thus the pulse fraction is found to increase with decay in the outburst.

5.3.3 Spectral Analysis

The three *NuSTAR* observations namely, Obs1, Obs2 and Obs4 were close to three *Swift* observations having Obs Ids 00088846001, 00088849001 and 00088870001 respectively. So we fitted *Swift*-XRT and *NuSTAR* (FPMA & B) spectra simultaneously in the 0.5-79.0 keV energy range, here *Swift* spectra were in 0.5-10 keV energy range and *NuSTAR* in 3-79 keV range. However there is a slight mismatch between the *Swift*-XRT and *NuSTAR* data points while fitting their spectra simultaneously, which has been reported earlier by Bellm *et al.* (2014). A CONSTANT model was used while fitting XRT and *NuSTAR* spectra

Table 5.2 Variation of pulse fraction (%) with energy four different observations.

Energy (keV)	Obs1	Obs2	Obs3	Obs4
5	3.85±0.15	11.92±0.02	3.22±0.01	6.28±0.01
8.5	5.89±0.01	12.98±0.34	5.13±0.01	10.08±0.03
9.5	6.63± 0.01	13.32±0.03	5.01±0.01	8.01±0.02
12	10.14±0.02	14.83±0.05	6.42±0.03	12.92±0.02
15	14.60±0.06	15.81±0.03	6.75±0.03	10.62±0.02
17	17.97±0.09	20.11±0.06	6.59±0.11	14.79±0.07
21	21.12±0.17	26.67±0.02	7.20±0.01	12.70±0.01
23	22.25±0.22	28.86±0.03	8.41±0.01	17.12±0.02
26	26.40±0.46	36.56±0.66	12.28±0.25	16.54±0.03
28	26.34±0.40	32.89±0.51	11.78±0.23	16.54±0.25
30	30.24±0.82	34.44±1.00	14.27±0.52	17.8±0.51

simultaneously to take into account the instrumental uncertainties and non-simultaneity of the observations. The spectra are fitted with two different combination of models. First we used the combination of CONSTANT, PHABS, BLACKBODY, CUTOFFPL and GAUSSIAN and in second case we replaced the CUTOFFPL with the model COMPTT which describes the Comptonization of soft photon in hot plasma. We define Model I to be framed as CONSTANT*PHABS*(CUTOFFPL+GAUSSIAN) and Model II as CONSTANT*PHABS*(COMPTT+GAUSSIAN). The cross section for the PHABS was chosen to be vern and the abundance was set to angr. The optical depth of the Comptonizing region in Model II was obtained using disk geometry. However in both the cases large negative residuals have been found near 10 keV. For this we have incorporated Gaussian absorption model GABS in both the cases. However, the HIGHECUT model did not fit the spectra well and consequently large residuals are observed near the cutoff energy.

When Model I was used to fit Obs1 and Obs2 without GABS model, a wave like feature in the residuals between 3-30 keV energy range have been found to exist with a large negative residuals near 10 keV, causing the fitting to be unacceptable (Fig. 5.6). However, addition of GABS model here fits the spectra well. The reduced χ^2 of the fitting were 1.76

Spectral parameters	Obs1+ <i>Swift</i>	Obs2+ <i>Swift</i>	Obs3	Obs4+ <i>Swift</i>
Model I				
n_H (cm ⁻²)	3.80±0.12	4.03±0.07	2.97±0.43	3.74±0.23
kT (keV)	0.17 ±0.04	0.23±0.02	0.31±0.05	0.15±0.07
α	0.51±0.02	0.46±0.02	0.34±0.01	0.80±0.02
E_H (keV)	7.26±0.12	6.82±0.02	6.21±0.08	6.87±0.02
E_{Fe} (keV)	6.52±0.03	6.52±0.07	6.49±0.02	6.61±0.08
σ_{Fe} (keV)	0.20±0.02	0.32±0.02	0.30±0.07	0.18±0.04
E_{gabs_1} (keV)	10.71±0.11	11.65±0.04	10.14±0.01	7.04±0.33
σ_{gabs_1} (keV)	4.32±0.12	2.49±0.09	4.12±0.14	6.54±0.23
τ_{gabs_1}	0.26±0.05	0.18±0.03	0.33±0.05	0.53±0.07
E_{gabs_2} (keV)	30.37±0.55	30.23±0.62
σ_{gabs_2} (keV)	1.79±0.34	1.04±0.35
τ_{gabs_2}	0.11±0.07	0.07±0.03
$flux$ (erg cm ⁻² s ⁻¹)	6.45 ^{+1.21} _{-0.61}	7.52 ^{+0.80} _{-0.74}	5.01 ^{+0.23} _{-0.1}	2.56 ^{0.90} _{-0.41}
χ^2_v	1.02	1.11	0.98	1.01
Model II				
n_H (cm ⁻²)	2.32±0.02	2.40±0.05	2.70±0.13	3.75±0.45
kT (keV)	0.27 ±0.05	0.39±0.04	0.47±0.02	0.28±0.08
T_0 (keV)	1.27±0.07	1.08±0.08	1.33±0.17	0.75±0.11
kT (keV)	4.81±0.05	4.58±0.05	4.52±0.06	4.63±0.11
τ	4.94±0.05	4.89±0.13	4.81±0.07	4.56±0.15
E_{Fe} (keV)	6.52±0.07	6.45±0.02	6.61±0.07	6.56±0.50
σ_{Fe} (keV)	0.27±0.05	0.23±0.04	0.24±0.04	0.22±0.05
E_{gabs_1} (keV)	11.32±0.36	10.87±0.03	9.57±0.64	10.03±0.27
σ_{gabs_1} (keV)	2.01±0.15	1.57±0.21	3.54±0.50	3.68±0.12
τ_{gabs_1}	0.09±0.04	0.07±0.02	0.17±0.05	0.14±0.07
E_{gabs_2} (keV)	30.09±0.57	31.18±0.48
σ_{gabs_2} (keV)	2.10±0.55	4.04±0.25
τ_{gabs_2}	0.15±0.07	0.10±0.06
$flux$ (erg cm ⁻² s ⁻¹)	6.41 ^{+0.51} _{-0.54}	7.49 ^{+0.61} _{-0.67}	4.15 ^{+0.45} _{-0.70}	2.51 ^{0.51} _{-0.25}
χ^2_v	1.01	1.11	1.00	0.99

Table 5.3 Best fitted spectral parameters of 4U 1901+03 for four different cases using Model I and Model II. α and E_H are photon index and highcut energy of the CUTOFFPL model. E_{gabs} and E_{Fe} are energy of absorption and Fe lines respectively. τ_{gabs} is the optical depth. σ_{gabs} and σ_{Fe} are the widths of absorption and Fe line. The subscript $gabs_1$ and $gabs_2$ are for two GABS models. The column density (n_H) and flux are in the scale of 10^{22} cm²² cm⁻² and 10^{-9} erg cm⁻² s⁻¹ respectively. T_0 , kT and τ are the spectral parameters of the COMPTT model. Flux were calculated in 3-79 keV energy range. Errors quoted are within 90% confidence interval.

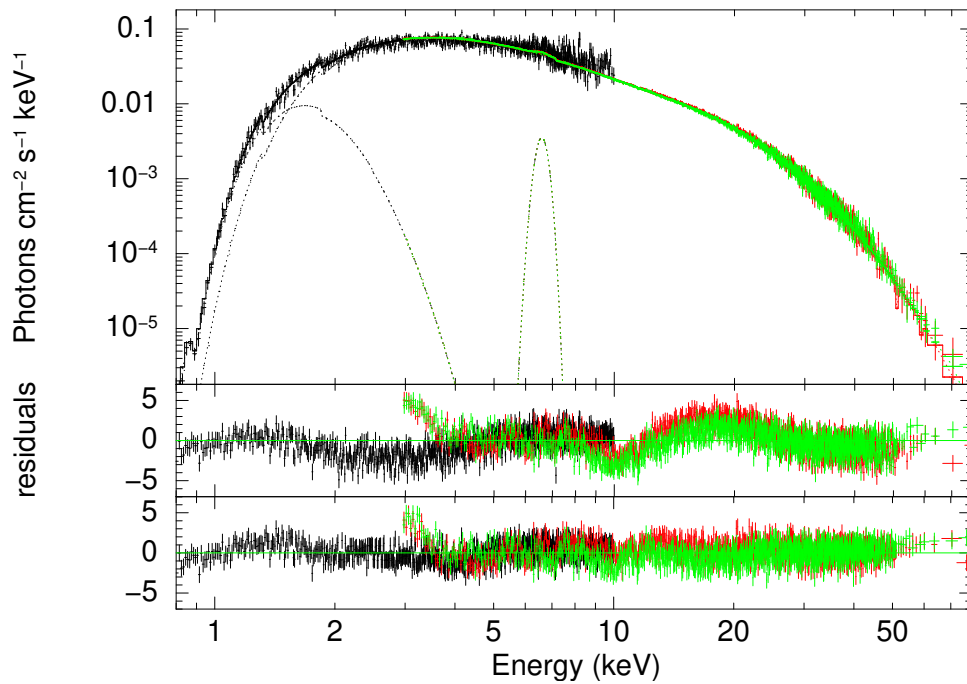


Fig. 5.6 Unfolded spectra of *NuSTAR* Obs1 and *Swift*-XRT observation fitted with Model I. The bottom and middle panels shows residuals after without and with the GABS model. Black indicates *Swift*-XRT spectra, red and green indicates *NuSTAR* FPMA & B spectra respectively.

and 1.52 for the first two cases respectively. However, after the addition of GABS model in the above we note that χ^2 values attained approximately 1.02 and 1.11 respectively.

During the *NuSTAR* Obs3 there was no *Swift* observations close to the *NuSTAR* observation timings, so we only fitted 3-79 keV FPMA & B spectra. The spectra were fitted well with Model I along with the GABS. As observed by Coley *et al.* (2019) we have found negative residuals near 30 keV indicating another absorption like feature and possibly a Cyclotron Resonant Scattering Feature (CSRF). Fitting this absorption like feature with GABS model Coley *et al.* (2019) found that the energy of the line to be at 31 keV with a width of 3.1 keV and optical depth about 1.1. So we have added another GABS model and searched for an absorption feature near 30 keV (see Fig. 5.7), the best fitted value of line energy was 30.37 keV. The width and the depth of the absorption lines are given by 1.79 keV and 0.11 respectively.

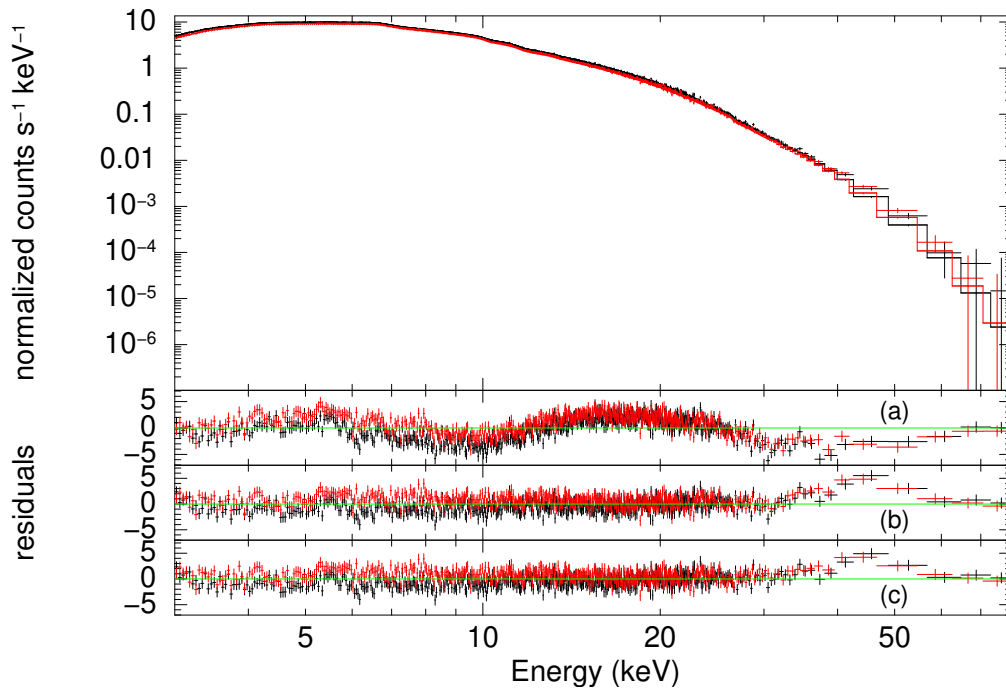


Fig. 5.7 Fitted spectra of *NuSTAR* Obs3 in 3-79 keV energy range. Panel (a) shows residuals for Model I where as panel (b) is residuals for Model I*GABS models and (c) shows residuals for Model I*GABS*GABS models.

The simultaneous fitting of *Swift*-XRT and *NuSTAR* Obs4 using Model I without GABS was not good as wave like feature has been observed with a large negative residuals near 10 keV. So we used two GABS models one for 10 keV and the other for 30 keV absorption like features, the spectra were fitted very well with the reduced $\chi^2 \sim 1.01$. However, the first absorption like feature was observed at 7.04 keV which is much below than what we have observed in the three previous cases. The second feature is observed at 30.23 keV with width and optical depth given by 1.04 keV and 0.07 respectively.

The spectra were also fitted well by Model II along with the GABS model. The column density is found to lie between $2.32\text{-}3.75 \times 10^{22} \text{ cm}^{-2}$ (Table 5.3). The input soft temperature (T_0) of COMPTT model varies between 0.75-1.33 keV. The plasma temperature (kT) and the plasma optical depth (τ) of the model are found to lie between 4.52-4.81 keV and 4.56-4.96 respectively. When the 10 keV feature was fitted with an absorption model the line energy was found at 11.32 keV, 10.87 keV, 9.57 keV and 10.03

keV for the four *NuSTAR* observations respectively. The width and the optical depth of this feature are in the range of 1.57-4.02 keV and 0.07-0.17 respectively. An absorption like feature around 30 keV was also observed in Obs3 and Obs4, so we used another GABS model here and observed that the line energies of the feature are 30.09 and 31.18 keV respectively.

From the spectral fitting by Model I we estimated the blackbody temperature to be about 0.20-0.31 keV. The iron emission line was estimated to lie between 6.52-6.61 keV. For all the four cases the flux were estimated in 3-79 keV energy range. The best fitted spectral parameters are shown in Table 5.3. The thermal component was also observed in the spectra fitted with Model II. The estimated flux were 6.45×10^{-9} , 7.52×10^{-9} , 5.01×10^{-9} and 2.56×10^{-9} erg cm⁻² s⁻¹ respectively. Thus the luminosity of the pulsar in 3-79 keV were $1.24 \times 10^{37} D_4^2$, $1.44 \times 10^{37} D_4^2$, $9.59 \times 10^{36} D_4^2$ and $4.89 \times 10^{36} D_4^2$ erg s⁻¹ for four all the four cases respectively. The 10 keV absorption like feature shows dependence on flux or luminosity and it increases or decreases with an increase or decrease in flux or luminosity, evident from Table 5.3, we noted that as flux decreases from 7.52×10^{-9} to 2.56×10^{-9} erg cm⁻² s⁻¹ the line energy of the feature decreases from 11.65 to 7.04 keV. Thus the line energy of the feature shows positive correlation with the source luminosity. The absorption feature near the 30 keV was only observed in the last two *NuSTAR* observations. This feature was also present in the spectra fitted with Model II. However when the spectra are fitted with Model II, the 10 keV feature does not show similar variation with the flux or the luminosity as seen in the case of spectral fitting with Model I but it shows positive correlation with either flux or luminosity. The observed flux and E_{Fe} were almost same in the two cases. We also fitted the spectra of the last two *NuSTAR* observations with the self-consistent Compton reflection models like PEXRAV, PEXRIV etc., however it is found that these models are not consistent with the observed spectra of the pulsar.

Fitting of Swift-BAT spectra

The 0.5-10 keV *Swift*-BAT spectra were fitted with PHABS and POWERLAW models. The power law model fits the spectra well and no additional models are required. As the pulsar slowly fades, the photon index increase or in other words with the decrease in flux the photon index increases (Fig. 5.9). Thus the spectra were softer near the end of the outburst. As the flux varies between $(0.13-39.60) \times 10^{-10}$ erg cm⁻¹ s⁻¹ the photon index varies between 1.03-2.1. The column density was observed to lie between $(3.20-4.31) \times 10^{22}$ cm⁻². The softening of the spectra of the pulsar at the end of an outburst was also observed by Reig and Milonaki (2016).

Phase Resolved Spectral Analysis

In order to understand the variation of spectral parameters with the pulse phase we have performed phase resolved spectral analysis of the *NuSTAR* observations. For phase resolved spectral analysis we have divided each pulse period into 10 equal segments (Fig. 5.8). For each segment a good time interval (*gti*) is created using XSELECT and then using this (*gti*) file FPMA & B spectra were produced. Each of the spectrum was fitted in 3-79 keV energy range with CONSTANT, PHABS, CUTOFFPL, GAUSSIAN and GABS models. Flux is then determined in 3-79 keV energy band. Spectral parameters are found to vary significantly with the phases. From the phase-resolved spectroscopy of Obs1 we observed that the photon index (α) and the highcut energy (E_H) shows anti-correlation with the flux. The flux varies between $(6.40-7.02) \times 10^{-9}$ erg cm⁻² s⁻¹ where as α and E_H varies between 0.19-0.366 and 6.08-6.64 keV respectively. The column density lies between $(0.80-1.54) \times 10^{22}$ cm⁻². The variation of the Fe emission line (E_{Fe}) follows complex pattern, its value decreases from 6.56 to 6.44 keV and then increases from 6.52 to 6.6 keV in between phase 0.2 to 0.6 and then decreases once again, however, an abrupt increase in its value is observed between 0.9-1.0. The absorption like feature (E_{gabs_1}) was also

observed which indicates anti-correlation with the flux that lies between 10.12-11.02 keV. However the width (σ_{gabs_1}) and optical depth (τ_{gabs_1}) of the line are found to have two peaks and also shows anti-correlation with the E_{gabs_1} and lies between 3.23-5.08 keV and 0.15-0.34 respectively.

From the phase-resolved spectral analysis of Obs2 (second column Fig. 5.8), the photon index and E_H show positive correlation with the flux. In this case the flux decreases in between 0.0-0.3 from 7.89×10^{-9} to 7.79×10^{-9} erg cm⁻² s⁻¹, but in between 0.4-0.8 the the flux increases reaching a maximum value 8.1×10^{-9} erg cm⁻² s⁻¹ at 0.7-0.8. The variation of the Fe line with the phase is found to be complex. The absorption feature E_{gabs_1} in between the phases 0.0-0.1 is 11.38 keV and it reaches a maximum value of 11.6 keV in between 0.1-0.2, thereafter it decreases reaching a minimum of 11.07 keV at 0.9-1.0. σ_{gabs_1} from 2.65 keV at 0.0-0.1 increases to attain a value of 3.12 keV after that it decreases to a minimum value of 2.06 keV in between phase 0.5-0.6, which thereafter increases followed by a decreasing behavior once again. The maximum value of σ_{gabs_1} is 3.50 keV and it was observed at 0.7-0.8. The optical depth (τ_{gabs_1}) decreases from 0.15 at 0.0-0.1 to 0.10 at 0.6-0.7 and then increases abruptly to 0.17, after which it decreases again. The column density varies between $1.14-1.77 \times 10^{22}$ cm⁻².

In Obs3 the variation of flux with phase is such that it exhibits two peaks one in between the phase 0.2-0.3 and the other in between 0.7-0.8. The photon index and E_H follows from the flux and it too has two peaks. The Fe line from 6.58 keV decreases to reach a minimum value 6.43 keV in the phase interval 0.2-0.3 and then it increases to climb a first peak value in the interval 0.5-0.6, after that it again decreases and then increases once again to reach a maximum value of 6.61 keV in the interval 0.9-1.0. From the Fig. 5.8 we can see that the variation in E_{gabs_1} is quite different from the two previous cases. The energy of the 10 keV feature E_{gabs_1} decrease from 9.87 keV in between 0.0-0.3 followed by an increase and thereafter a decrease. In the interval 0.4-0.6 the value E_{gabs_1} increases again followed by a

sharp decrease reaching 8.57 keV and after that it increases again. It is evident from the Fig. 5.8 the width of the line σ_{gabs_1} shows negative correlation with the E_{gabs_1} . The optical depth (τ_{gabs_1}) does not vary much in the phase interval 0.0-0.6. In this case the column density varies between $(0.38-1.72)\times 10^{22}$ cm⁻².

From the phase-resolved spectral analysis of the fourth *NuSTAR* observation we found that the flux lies between $(2.53-2.72)\times 10^{-9}$ erg cm⁻² s⁻¹. The minimum value of photon index 0.39 was observed at phase interval 0.4-0.5 and the maximum value of 1.04 was observed at 0.5-0.6. The cutoff energy (E_H) was within 5.94-7.09 keV energy range. The value of the column density (n_H) lies between $(1.54-3.63)\times 10^{22}$ cm⁻¹. The iron fluorescence line was lying between 6.45-6.64 keV with its width in 21-380 eV energy range. The 10 keV feature is found to vary between 5.84-8.79 keV. The width and the optical depth of the feature were lying between 1.97-5.59 keV and 0.68-0.99 respectively.

The absorption like feature at 30 keV in Obs3 is found to depend on the pulse phase (Fig. 5.10). The estimated line energy increases from 29.38 to 38.24 keV between the phase interval 0.0-0.4 which decreases to 33.38 keV, after that it increases once again to 33.88 keV and then decreases again to 30.33 keV. In the phase interval 0.7-1.0 the line energy increases as follows 29.89-36.21 keV. The width σ_{gabs_2} and optical depth τ_{gabs_2} of the feature are found to vary with the pulse phase and found to lie between 2.17-7.16 keV and 0.2-0.7 respectively. For the Obs4, the 30 keV feature was found to vary between 27.6-33.51 keV with its width lying between 3.29-6.41 keV and depth varying between 0.17-0.42 (Fig. 5.10).

The phase resolved spectra of Obs1 and Obs2 is fitted with additional GABS model in order to look for the presence of 30 keV absorption like feature. For Obs1 the line energy and the width of the feature were found to vary between 31.24-38.76 keV and 0.75-6.15 keV respectively and it is noted that the feature is not visible in the phase intervals 0.7-0.8 and 0.8-0.9. In the case of Obs2, the energy of the feature lies between 28.90-35.48 keV

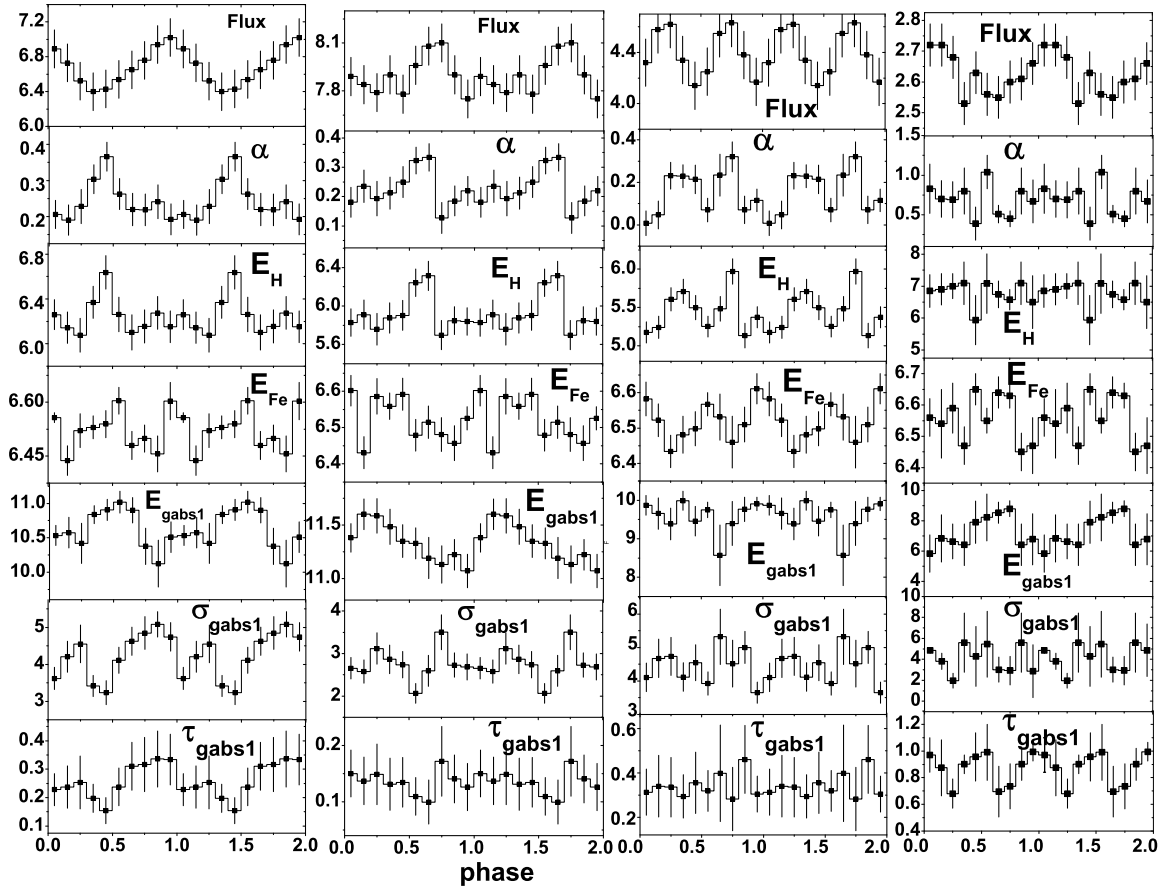


Fig. 5.8 Variation of Spectral parameters with pulse phases for four *NuSTAR* observations. Figures in first, second and third columns are for Obs1, Obs2, Obs3 and Obs4 respectively. α and E_H are photon index and highcut of CUTOFFPL model. E_{Fe} is the energy of Fe line. E_{gabs1} , σ_{gabs1} and τ_{gabs1} are the line energy, width and optical depth of GABS model used for fitting 10 keV feature.

with width between 0.77-6.06 keV. However for phase intervals 0.5-0.6 and 0.8-0.9 of Obs2 as the value of σ_{gabs2} and τ_{gabs2} are unrealistic so we did not consider them here for analysis.

5.4 Discussion

We present the Be X-ray pulsar 4U 1901+03 analysis, which was undergone short bursts of tens to hundreds of seconds. The burst of the X-ray pulsar can be due to instability

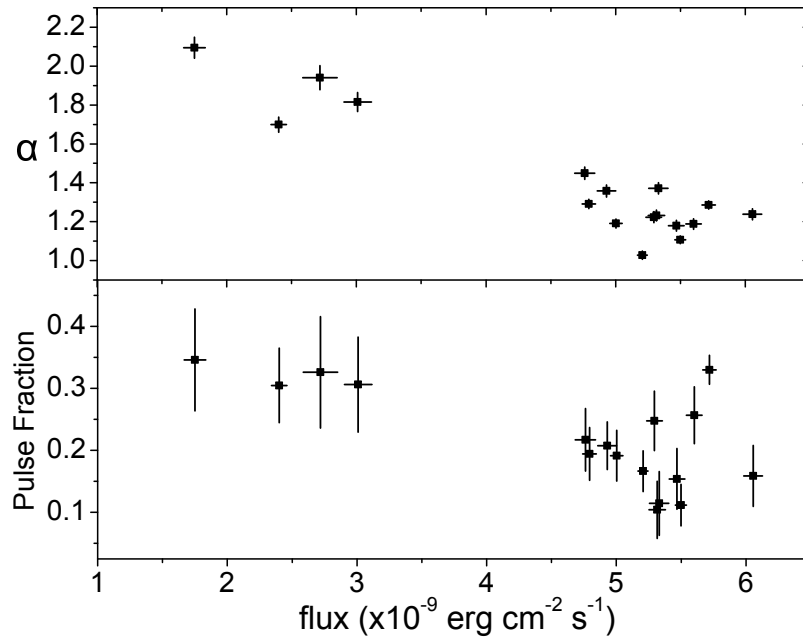


Fig. 5.9 Variation of photon index and pulse fraction with *Swift*-XRT flux in 0.5-10 keV energy range.

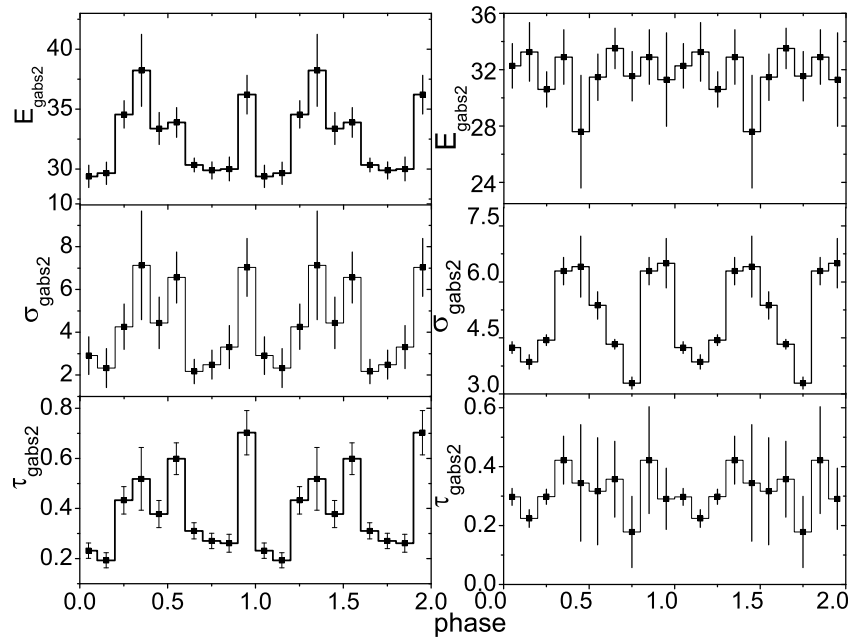


Fig. 5.10 Variation of 30 KeV absorption feature with phase for Obs3 (first column) and Obs4 (second column). E_{gabs2} , σ_{gabs2} and τ_{gabs2} are the line energy, width and the optical depth of the feature.

in accretion disk burst (Taam *et al.* (1988); Lasota and Pelat (1991); Cannizzo (1996)) similar to the burst observed in other sources namely, SMC X-1, GRO J1744-28 and MXB 1730-355 (Moon *et al.* (2003); Rai *et al.* (2018); Briggs *et al.* (1996); Lewin *et al.* (1976)). Pulse profiles shows variation with both the time and the flux, which are similar to that observed by Lei *et al.* (2009), Reig and Milonaki (2016) and Ji *et al.* (2020). The bursts in this case are different from the thermonuclear burst which is characterized by sharp rise and exponential decay. From the *NuSTAR* observations we found that the pulse profile having a single peak evolved into double peak with one main peak and once again become single peaked (Fig 5.3). Similar variations have been observed in *Swift*-XRT pulse profiles (Fig. 5.4). The height of the pulse profile peak increases with the increase in energy. Also the double peaked pulse profile in Obs2 evolved into single peak at the hard energy range. The pulse fraction is found to increase with the increase in energy at the end of the outburst. As the X-ray emitting region shrinks with the increase in energy, it emits more pulses as a result the pulse fraction increases (Alexander and Sergey, 2008). The variation of the pulse profiles may be due to a change in the accretion regimes. The different accretion regimes are set by the critical luminosity (Basko and Sunyaev, 1976; Becker *et al.*, 2012; Mushtukov *et al.*, 2015). The critical luminosity (L_{crit}) is defined as the luminosity above which the radiation pressure is strong enough to stop the accreting matter at a certain distance above the neutron star. The super-critical regime is reached when the luminosity of the pulsar (L_X) is greater than L_{crit} . In this case radiation dominated shock wave is formed which moves up to few kilometers above the neutron star. However for sub-critical regime $L_X < L_{crit}$, accreting material are capable of reaching onto the surface of the neutron star with heating it. In the case of the super-critical regime, X-ray photons escape from the side surface of the accretion column perpendicular to the magnetic field lines thus forming fan shaped beam but for sub-critical regime the emission is parallel to the magnetic field which comes out as a pencil beam pattern consisting of pulsed component

with simple pulse profile. The pulse profile associated with the fan shaped beam pattern is however complex in shape and in some cases it may be a mixture of fan and pencil shape beam as predicted. The abrupt change in the correlation of the photon index with the flux also indicates a transition from super-critical regime to sub-critical regime (Reig and Nespoli, 2013).

From the *NuSTAR* observations we observed that the pulse profile (Fig. 5.3) is sinusoidal in shape at a luminosity of $1.22 \times 10^{37} D_4^2$, which evolved into double-peak pulse profile with one main peak at $1.43 \times 10^{37} D_4^2 \text{ erg s}^{-1}$. The second peak of the pulse profile however disappear and becomes a single-peak with a notch near ~ 0.5 when the luminosity of the pulsar becomes $9.59 \times 10^{36} D_4^2 \text{ erg s}^{-1}$. With the further decrease in luminosity the notch disappears and pulse profile become single peak again which is found at $2.44 \times 10^{36} D_4^2 \text{ erg s}^{-1}$. Similar variations are observed in *Swift*-XRT pulse profiles (Fig. 5.4).

Thus 4U 1901+03 shows luminosity dependent pulse profile having a double peak at high luminosity and single peak at low luminosity. The complex variation of pulse profiles can be due to change in emission beam pattern with luminosity, which may be a mixture of fan and pencil beam pattern (Chen *et al.*, 2008; Ji *et al.*, 2020; Reig and Milonaki, 2016). The mixed contribution of the fan and pencil beam suggest that the source was not in pure super-critical regime during the recent outburst and most of the time it was in the sub-critical regime (Chen *et al.*, 2008; Reig and Milonaki, 2016). In the analysis carried out here no abrupt change in the correlation between the flux and photon index is seen supporting the fact that the source was in the sub-critical regime of accretion.

The 10 keV absorption like feature of the source was observed in all the four *NuSTAR* observations and it increases significantly with the increase in luminosity. Also the width and optical depth of the feature varies for different observations. The energy, width and the optical depth of the feature are found to lie within the range observed by Reig and Milonaki (2016). It was observed that accreting pulsars show positive correlation of the

cyclotron line energy with the luminosity in the sub-critical regime and negative correlation in the super-critical regime (Becker *et al.*, 2012; Mushtukov *et al.*, 2015). If the pulsar was in sub-critical regime most of the time during the outburst as discussed above then the observed positive correlation of the 10 keV feature indicates a cyclotron line. In addition to that the strong dependence of this feature on the viewing angle *i.e.* on the pulse phase like cyclotron line which also shows strong dependence on the pulse phase (Heindl *et al.*, 2004; Isenberg *et al.*, 1998; Reig and Milonaki, 2016), which pointed that this feature is due to a cyclotron line. The width and optical depth of the 10 keV features are within the range given by Coburn *et al.* (2002) for other pulsars. The 10 keV feature are observed in pulsars having CRSF or not at all but it is found to depend on the pulse phase (Coburn *et al.*, 2002). Considering the canonical value of neutron star parameters, the theoretical calculated value of critical luminosity by Becker *et al.* (2012) satisfy $L_{crit} \sim 1.49 \times 10^{37} B_{12}^{16/15}$, thus for this feature to be CRSF it is accepted that the critical luminosity must be $\sim 10^{37}$ erg s⁻¹. Assuming the distance of the source to be 3 kpc Bailer-Jones *et al.* (2018), the estimated observed luminosity is found to lie between $2.69-8.04 \times 10^{36}$ erg s⁻¹ which is however below the critical luminosity. Reig and Milonaki (2016) noted that for the $\frac{L_{peak}}{L_{crit}} \sim 1$, the distance should not be larger than ~ 4 kpc. Thus for the estimated luminosity less than the critical luminosity the distance of the source must be less than 4 kpc. However Strader *et al.* (2019) noted that the distance of the object measured by the Bailer-Jones *et al.* (2018) was not well constraint because of the parallax of the star in Gaia DR2 which was insignificant and considering PS1 reddening maps along the direction of the source (Green *et al.*, 2018) concluded that the distance must be greater than 12 kpc. Recently Tuo *et al.* (2020) with the help of torque model and evolution of pulse profile during outburst the estimated distance of the source is found to be 12.4 kpc. Assuming the distance of the source as 12.4 kpc the observed luminosity can be calculated and which lies between $(4.59-13.74) \times 10^{37}$ erg s⁻¹. The measured value is close to or above the critical luminosity and it raises a doubt about

this feature being CRSF. Mushtukov *et al.* (2015) showed that the critical luminosity is not a monotonic function of magnetic field and for the pulsars having cyclotron energy about 10 keV the critical luminosity can reach a minimum value of few 10^{36} erg s⁻¹. If this is the case then even if the source be at a distance of 3 kpc the observed luminosity will be equal or greater than the critical luminosity. In *NuSTAR* spectra weak residuals are observed around 10 keV due to tungsten L-edge of the *NuSTAR* optics (Fürst *et al.*, 2013; Madsen *et al.*, 2015). The 10 keV features were present in the spectra of various X-ray pulsars obtained using different instruments of different satellites (Coburn *et al.*, 2002) like in the case of 4U 1901+03 where this feature has been observed by RXTE (Reig and Milonaki, 2016) and *Insight-HMXT* (Nabizadeh *et al.*, 2020), thus it cleared a doubt about the instrumental origin of the feature. We have also seen that the feature is present even if we used another continuum model COMPTT instead of CUTOFFPL. Nabizadeh *et al.* (2020) showed that when *NuSTAR* Obs3 spectra were fitted by two-components model consisting of two POWERLAW*HIGHECUT along with GAUSSIAN and PHABS models no residuals were left near 10 keV and also no additional absorption model around 10 keV found when this two component model was used to fit *Insight-HMXT* spectra. However the authors also argued that the transition from the typical cutoff power-law spectral shape to two-component spectral shape occurs at low luminosities about $10^{(34-36)}$ erg s⁻¹, which indicates that the source distance must be small. Thus without proper estimation of the distance it is not sure about the feature to be CSRF. It is equally possible that this feature be inherent feature of the accreting X-rays pulsars or due to departure of the phenomenological models used in fitting the spectra Coburn *et al.* (2002).

As observed by Nabizadeh *et al.* (2020) and Coley *et al.* (2019) when Obs3 and Obs4+*Swift* spectra were fitted some negative residuals were observed near 30 keV, fitting the spectra with additional absorption model we have estimated the line energy that lies at 30.37 and 30.23 keV for these observations respectively and these are consistent with

the values estimated by Nabizadeh *et al.* (2020) and Coley *et al.* (2019). However no negative residuals near 30 keV were observed in the first two *NuSTAR* spectra which were having higher flux compared to the last two observations. In Obs3 and Obs4 the line energy of 30 keV feature showed pulse phase variation. Despite the fact that this feature was not observed in the phase-averaged spectra of Obs1 and Obs2 it was observed in the phase-resolved spectra of these observations. However in Obs1 and Obs2 this feature was not observable in some phases. Beri *et al.* (2021) confirmed existence of this feature to be due to cyclotron line by studying the variation of the line energy with the luminosity and the pulse phase. They observed an abrupt change in the pulse profiles around the line energy of the feature. In X-ray pulsars with high mass accretion rate the accretion columns will appear to be confined by the strong magnetic field of the neutron star and supported by the internal radiation pressure. Thus observed cyclotron line can be originated from the accretion column (Schönherr *et al.*, 2014) or due to the X-rays reflected from the neutron star atmosphere (Poutanen *et al.*, 2013). The absence of the cyclotron line in some observed energy spectra of the XRBs can possibly due to large gradient of B-field strength over the visible column height or the latitude on the surface of the neutron star. The appearance of the cyclotron line in certain pulse phases can be due to the partial eclipsing of the accretion column during which an observer is not able to see some parts of the column (Molkov *et al.*, 2019). In such case the magnetic field in the visible part of the accretion column is not so varied and one can observe cyclotron line in these phases like in the case of GRO J2058+42 (Molkov *et al.*, 2019). The appearance of cyclotron line only in some specific phases can be due to the gravitational bending of light too, as it affects the visibility of both the accretion columns and neutron star (see eg. Mushtukov *et al.* (2018)).

When the magnetospheric radius r_m becomes greater than the co-rotational radius r_{co} then the centrifugal force will prevent the material from further falling onto the neutron star, this is known as *Propeller Effect* (Illarionov and Sunyaev, 1975; Stella *et al.*, 1986)).

As the propeller effect sets in there will be an abrupt decrease in the flux leading to an absence of pulsation and even cause non-detection of source. Here the co-rotational radius is defined as the radius where the Keplerian angular velocity is equal to the spin angular velocity of the neutron star. The magnetospheric radius depends on the mass accretion rate, during the bright phase of an outburst the magnetospheric radius is less than the co-rotational radius consequently matter can cross the magnetospheric region and reach the neutron star. As the mass accretion rate decreases the magnetospheric radius increase thereby it can reach a point when its radius equal to the co-rotational radius, the propeller phase sets in at this stage. From the NICER observations it was detected that there does not exist pulsation after 58665.09 MJD, and the flux abruptly decreases from 6.37×10^{-10} at 58637.08 MJD to 1.31×10^{-11} erg s⁻¹ at 58667.45 MJD which indicates that the pulsar entered into the propeller phase. The increase in pulse fraction and the softening of the spectrum at the end of the outburst also supports our argument (Reig and Milonaki, 2016; Tsygankov *et al.*, 2016; Zhang *et al.*, 1998). As the accretion of matter onto the neutron star ceases at $r_m = r_{co}$, the magnetic field in this case can be determined, which is given by $B = 4.8 \times 10^{10} P^{7/6} \left(\frac{flux}{10^{-9} \text{ ergs}^{-1}} \right)^{1/2} \times \left(\frac{d}{1 \text{ kpc}} \right) \left(\frac{M}{1.4 M_{\odot}} \right)^{1/3} \left(\frac{R}{10^6 \text{ cm}} \right)^{-5/2}$ G (Cui, 1997)), where *flux* represents the minimum bolometric X-ray when the pulsation was still detectable and *d* represents the distance to the source. Using *Swift*-XRT *flux* 6.37×10^{-10} erg cm⁻² s⁻¹ in 0.5-10.0 keV observed at 58637.08 MJD and it was the minimum flux estimated in *Swift*-XRT observations when the source was still pulsating, assuming the distance to the source to lie between 3-12.5 kpc, the estimated magnetic field of the neutron star lies $(0.38-1.56) \times 10^{12}$ G, making use of the canonical values of mass and radius. However, the estimated magnetic field is entangled with uncertainties because the bolometric correction of the flux was not done and the minimum flux measured in the observation was not exactly known.